Nano Research

ISSN 1998-0124 CN 11-5974/O4
https://doi.org/10.26599/NR.2026.94908747

Research Article

Surface-engineered porous aromatic framework enables a monolithic aerogel for high-efficiency benzene adsorption

Qihaoyue Wang, Yao Zheng, Wei Hu, Jiangtao Jia(✉), Guangshan Zhu(✉)
Key Laboratory of Polyoxometalate and Reticular Material Chemistry of Ministry of Education, Faculty of Chemistry, Northeast Normal University, Changchun 130024, China

Nano Res., **Just Accepted Manuscript** • https://doi.org/10.26599/NR.2026.94908747
https://www.sciopen.com/journal/1998-0124 on Apr. 17, 2026

Just Accepted

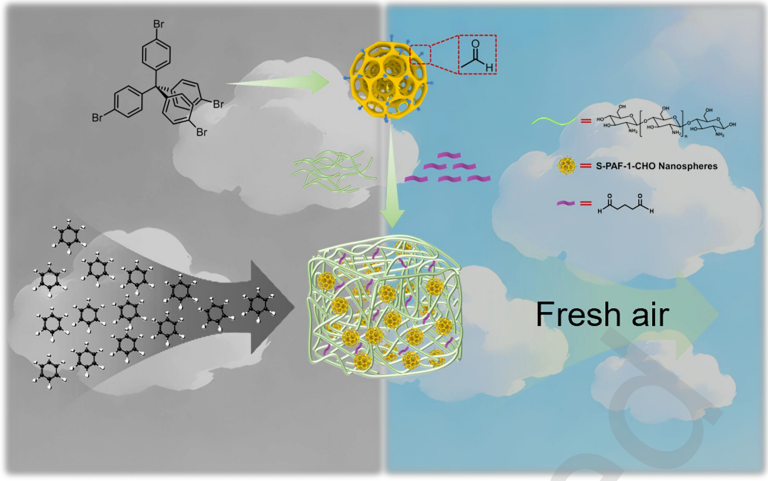

This study addresses the inherent trade-off between mechanical strength and adsorption capacity that has long plagued shaped sorbents, establishing a general approach to convert fragile porous powders into robust monoliths suitable for practical applications.

Nano Research

Open Access

Research Article

Surface-engineered porous aromatic framework enables a monolithic aerogel for high-efficiency benzene adsorption

Qihaoyue Wang, Yao Zheng, Wei Hu, Jiangtao Jia, and Guangshan Zhu

Key Laboratory of Polyoxometalate and Reticular Material Chemistry of Ministry of Education, Faculty of Chemistry, Northeast Normal University, Changchun 130024, China

Received: 2 March 2026; **Revised:** 16 April 2026; **Accepted:** 17 April 2026

Address correspondence to Jiangtao Jia, jiangtaojia@nenu.edu.cn; Guangshan Zhu, zhugs@nenu.edu.cn

Cite this article: *Nano Research*, 2026, 19, 94908747 https://doi.org/10.26599/NR.2026.94908747

ABSTRACT: Transforming fragile porous powders into robust, engineered monoliths without compromising the major porosity remains a key challenge. Herein, we address this by developing a surface-selective modification strategy that grafts aldehyde groups solely onto the external surface of porous aromatic framework-1 (PAF-1), yielding S-PAF-1-CHO. This modification preserves its pristine 1.4 nm micropores while enabling covalent integration with chitosan via Schiff-base chemistry to form lightweight aerogels with a high S-PAF-1-CHO loading. The resulting monolithic sorbent maintains a high specific surface area, great mechanical stability and achieves an exceptional benzene adsorption capacity of 5.98 mmol g^{-1} (2000 ppm). This work establishes a versatile paradigm for converting high-capacity porous powders into practical, shaped sorbents through precise interfacial engineering.

KEYWORDS: porous organic polymers, porous aromatic framework, benzene adsorption, aerogel; volatile organic compounds

1 Introduction

Volatile organic compounds (VOCs) are a major class of air pollutants, encompassing a wide range of organic species, including benzene derivatives (such as benzene, toluene, ethylbenzene, and xylenes), as well as aldehydes, ketones, olefins, ethers, and related compounds [1]. Among these, benzene derivatives mainly arise from industrial chemical waste and pose significant risks to both environmental quality and human health [2]. In particular, benzene is recognized as one of the most toxic VOCs and widely exists in both indoor and outdoor environments. Its emission sources include a range of commonly used products, such as gasoline, tobacco, paints, and adhesives [3, 4]. Extensive evidence has demonstrated that long-term exposure to benzene can induce dizziness, nausea, irritation of the eyes and skin, respiratory damage, and even carcinogenic effects [5, 6]. Accordingly, the efficient removal and recovery of benzene from air are of great significance for environmental protection and public health.

Among the various recovery methods, adsorption is considered an economically feasible approach owing to its low energy consumption, cost-effectiveness, and high efficiency [7-9]. The selection of appropriate adsorbents is a critical step in adsorption-based processes. Conventional adsorbents, such as zeolites, resins, and activated carbons, have been widely employed; however, their relatively low surface areas and limited porosities often lead to insufficient adsorption capacities [10-12]. Therefore, the development of highly efficient benzene adsorbents is of great importance. Porous aromatic frameworks (PAFs), a subclass of porous organic polymers (POPs), feature exceptionally high surface areas, well-developed porosity, and excellent structural stability, and have been widely explored for gas adsorption and separation, catalysis, and the capture of chemical species [13-16]. The aromatic rings and stable C–C covalent linkages in PAFs confer them hydrophobicity and a well-defined framework structure. These features allow PAFs to overcome the limitations of conventional adsorbents while providing unique advantages for benzene adsorption.

Most porous framework materials are available only as fine powders; however, practical applications require monolithic structures with well-defined shapes, sufficient hardness, and mechanical robustness. Powdered adsorbents are challenging to handle, exhibit poor mechanical stability, and can lead to significant pressure drops in adsorption columns [17]. Therefore, the development of shaped adsorbents that combine enhanced mechanical durability with the preservation of excellent benzene adsorption performance is of considerable importance. In previous studies, shaped adsorbents targeting aromatic VOCs have often suffered from low powder loadings, significant reductions in surface area, and synthetic challenges, all of which compromise their adsorption performance [17-25].

In this work, an aldehyde-functionalized PAF-1 material (S-PAF-1-CHO) was synthesized via an unconventional surface-modification strategy. Compared to traditional post-synthetic modification methods for porous frameworks, where both the interior and exterior surfaces are modified, this strategy introduces reactive aldehyde sites exclusively

on the external particle surface. This preserves the parent framework's high surface area and provides connecting sites for cross-linking with aerogel agents. These groups were subsequently utilized to react with the amino groups of chitosan, enabling the fabrication of mechanically stable S-PAF-1-CHO@CS aerogels with a high powder loading of up to 80 wt%. Importantly, the resulting aerogels retain excellent benzene adsorption capacity and demonstrate enhanced performance under dynamic adsorption conditions.

2 Experimental

2.1 Materials and instrumentations

Unless otherwise specified, all materials and solvents used in the experiments were purchased from Innochem Co.

Fourier transform infrared (FT-IR) spectra were recorded on a Nicolet iS10 spectrometer in the range of 400-4000 cm^{-1} using KBr pellets. Solid-state ^{13}C nuclear magnetic resonance (^{13}C NMR) spectra were measured on a Bruker Avance III 500 MHz NMR spectrometer. Scanning electron microscopy (SEM) images were obtained using a Hitachi SU-8010 microscope at an accelerating voltage of 3 kV. Nitrogen adsorption-desorption isotherms at 77 K and vapor adsorption isotherms were measured on Autosorb analyzers (JW-TB 400 and JW-ZQ 100). Vapor adsorption measurements at 298 K were conducted using a Autosorb analyzers (JW-ZQ 100 C). Thermogravimetric analysis (TGA) was performed using a Mettler-Toledo TGA/DSC 3+ instrument under air atmosphere with a heating rate of 10 °C/min.

2.2 Synthesis of PAF-1

PAF-1 was synthesized following the procedure reported in the literature. In a glovebox, 1,5-cyclooctadiene (cod, 1.05 mL, 8.32 mmol), bis(1,5-cyclooctadiene) nickel(0) ($Ni(cod)_2$, 2.25 g, 8.18 mmol), 2,2'-bipyridine (1.28 g, 8.18 mmol), and anhydrous N,N-dimethylformamide (DMF, 60 mL) were added to a 250 mL two-necked round-bottom flask. The mixture was activated at 80 °C for 1 h. Subsequently, a DMF solution (60 mL) of tetrakis(4-bromophenyl)methane (1.00 g, 1.57 mmol) was slowly added dropwise to the mixture. The reaction was maintained at 80 °C for an additional 48 h. After cooling to room temperature, 6 M hydrochloric acid was added, and the mixture was stirred for 1 h until the solution turned green and a snowflake-like solid formed. The solid was collected, washed, and dried to obtain the target PAF-1 product.

2.3 Synthesis of S-PAF-1-CHO

S-PAF-1-CHO was synthesized in a glovebox. In a 100 mL two-necked flask (Flask A), tetrakis(4-bromophenyl) methane (0.60 g, 0.94 mmol) was added. In a 250 mL two-necked flask (Flask B), bis(1,5-cyclooctadiene) nickel(0) ([$Ni(cod)_2$], 1.44 g, 5.24 mmol), 2,2′-bipyridine (0.81 g, 3.68 mmol), and 1,5-cyclooctadiene (cod, 0.65 mL, 5.04 mmol) were added. In a 50 mL two-necked flask (Flask C), 2-(4-bromophenyl)-1,3-dioxolane (0.17 g, 0.77 mmol) was added. Then, 10 mL of DMF was added to Flask A, 90 mL DMF and 90 mL THF were added to Flask B, and 10 mL DMF and 10 mL THF were added to Flask C. Flask B was allowed to activate at room temperature for 1 h. The solution from Flask A was then added to Flask B. After 1 h, the solution from Flask C was added dropwise to Flask B over 30 min. The resulting mixture was stirred at room temperature for 48 h, yielding a dark purple suspension. The product was collected following the same procedure as PAF-1, and after vacuum drying, a white powdery solid was obtained.

2.4 Synthesis of S-PAF-1-CHO@CS Aerogels with Different Ratios

The preparation of the 60 wt% S-PAF-1-CHO@CS aerogel is presented as an example. Chitosan (15.0 mg) was dissolved in 3 mL of 1 vol% acetic acid aqueous solution. Subsequently, S-PAF-1-CHO powder (22.5 mg) was added to the chitosan solution and dispersed by sonication. Under continuous stirring, 3.5 μL of 50 wt% aqueous glutaraldehyde solution was added, and the mixture was stirred overnight. The resulting gel was then freeze-dried to obtain the aerogel.

2.5 Breakthrough Experiment Conditions

Before each experiment, the carrier gas flow rate and the temperature of the saturator were adjusted to achieve the desired benzene vapor outlet concentration and maintain stability. Approximately 100 mg of the sample was then loaded into the adsorption bed, which was maintained at 298 K. The sample was degassed at 100 °C overnight to remove physically adsorbed water molecules and other impurities. The benzene concentration was set to 2000 ppm, with a total gas flow rate of 25 $mL \cdot min^{-1}$.

3 Results and discussion

3.1 Synthesis of S-PAF-1-CHO and S-PAF-1-CHO@CS aerogel

To introduce aldehyde groups onto the surface of PAF-1, an end-capping strategy was employed. As illustrated in Figure 1a, a monodentate bromobenzene end-capping agent was added during the Yamamoto-type Ullmann coupling polymerization of PAF-1, thereby terminating the reaction. The intermediate product containing cyclic acetal units was subsequently hydrolyzed to yield the aldehyde-functionalized PAF-1, designated as S-PAF-1-CHO. The success of the end-capping reaction was confirmed by solid-state ^{13}C NMR and FT-IR analyses. In the FT-IR spectrum (Figure 1b), the characteristic C-Br stretching peaks at 512 and 532 cm^{-1} were absent in S-PAF-1-CHO [13], whereas a new peak appeared at 1712 cm^{-1}, corresponding to the C=O stretching vibration of aldehyde groups [26]. These observations confirm the successful grafting of aldehyde functionalities onto the PAF-1 surface. In the solid-state ^{13}C NMR spectrum (Figure 1c), the peaks at 140 and 133 ppm are attributed to unsubstituted aromatic carbons, while the peaks at 124 and 119 ppm correspond to aromatic carbons bearing hydrogen atoms. The peak at 58 ppm is assigned to the quaternary carbon atom connecting the four phenyl rings [13], and the peak at 182 ppm is assigned to the aldehyde carbon, further validating the successful synthesis of S-PAF-1-CHO [27]. Nitrogen adsorption–desorption isotherms for PAF-1 and S-PAF-1-CHO at 77 K are shown in Figure 1d. Their BET surface areas are 4575 and 3672 $m^2 g^{-1}$, respectively.

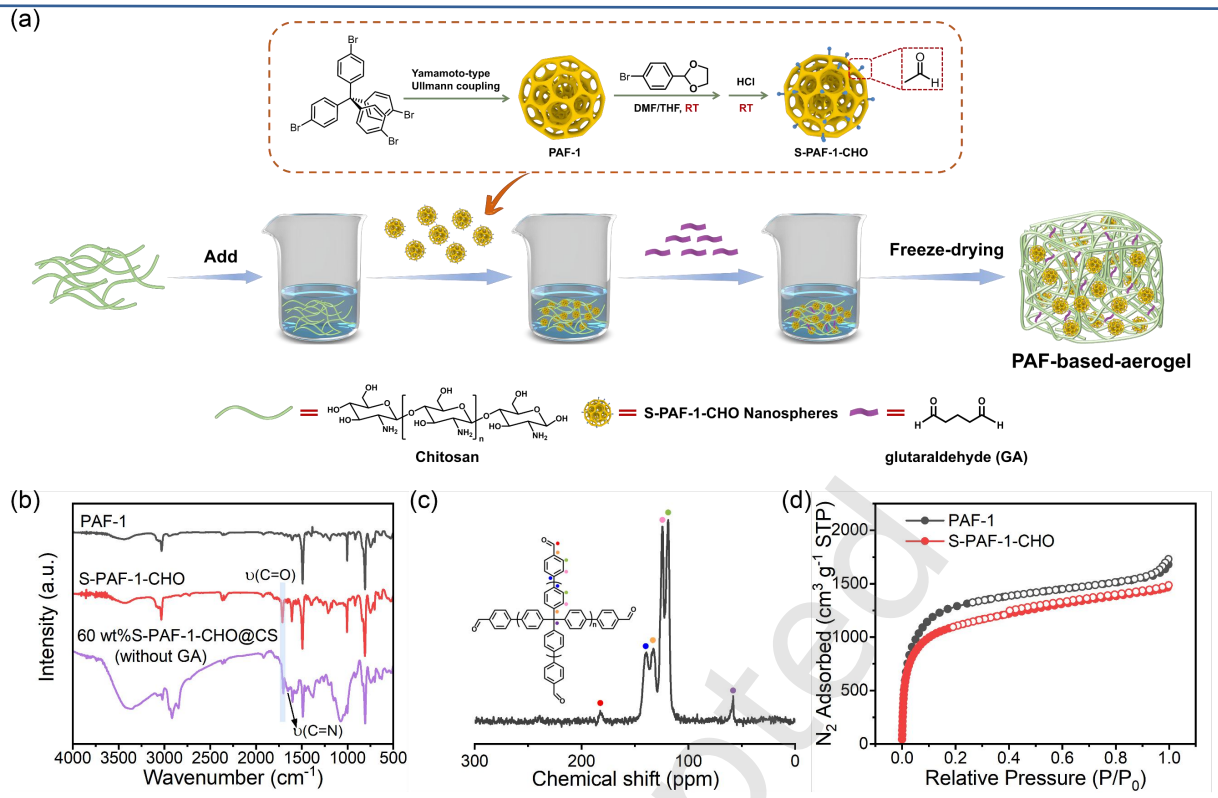

Figure 1. (a) Schematic illustration of the surface-modification strategy used to synthesize S-PAF-1-CHO and S-PAF-1-CHO@CS composite aerogels; (b) FT-IR spectra of PAF-1, S-PAF-1-CHO and 60 wt% S-PAF-1-CHO@CS (without GA) aerogel; (c) ^{13}C CP/MAS NMR spectrum of S-PAF-1-CHO; (d) N_2 adsorption-desorption isotherms of PAF-1 and S-PAF-1-CHO at 77 K.unchanged at 1.41 nm for both materials (Figure S1), indicating that the aldehyde groups are confined to the surface and do not occupy the internal pore channels.

Although the BET surface area of S-PAF-1-CHO exhibits a slight decrease relative to pristine PAF-1, the pore size distribution remains unchanged at 1.41 nm for both materials (Figure S1), indicating that the aldehyde groups are confined to the surface and do not occupy the internal pore channels. The chemical stability of S-PAF-1-CHO was further evaluated under harsh acidic and alkaline conditions. S-PAF-1-CHO was immersed in 6 M HCl and 1 M NaOH aqueous solutions overnight, respectively. FT-IR spectra (Figure S2) and 77 K nitrogen adsorption measurements (Figure S3) reveal that the characteristic peaks of S-PAF-1-CHO are well preserved, and the material still maintains a high BET surface area after acid and alkali treatment, indicating the outstanding acid-base stability of S-PAF-1-CHO.

Chitosan, a widely studied natural polymer, is attractive due to its low cost, non-toxicity, biodegradability, and ease of processing. Its abundant amino and hydroxyl functional groups further enable diverse applications [28]. In this study, chitosan was chosen to react with S-PAF-1-CHO for the fabrication of composite aerogels. To explore mechanically robust aerogels, an initial composite was prepared using S-PAF-1-CHO powder and chitosan with a 60 wt% filler content. As shown in the FT-IR spectrum in Figure 1b, the 60 wt% S-PAF-1-CHO@CS aerogel without glutaraldehyde (GA) exhibits a characteristic C=N stretching band at 1655 cm^{-1}, indicating the formation of Schiff bases between the aldehyde groups of S-PAF-1-CHO and the amino groups of chitosan[26]. However, compression stress-strain testing (Figure S4) revealed that this aerogel displayed poor mechanical durability. To enhance structural integrity, GA was introduced as an additional crosslinker. Figure 1a illustrates the final fabrication procedure of the S-PAF-1-CHO@CS composite aerogels. S-PAF-1-CHO powder was first dispersed into an acetic acid aqueous solution of chitosan to form a homogeneous suspension, allowing Schiff base reactions between S-PAF-1-CHO and chitosan to immobilize the S-PAF-1-CHO particles within the chitosan framework. GA was then added to the mixture to induce additional crosslinking with chitosan, thereby further reinforcing the network structure. Finally, a series of PAF-based aerogels were obtained via freeze-drying. When the powder loading was maintained at 60 wt%, the resulting 60 wt% S-PAF-1-CHO composite aerogel exhibited significantly higher compressive strength at 40% strain. By varying the mass ratio between S-PAF-1-CHO and chitosan, composite aerogels containing 60 wt%, 70 wt%, and 80 wt% S-PAF-1-CHO were fabricated, referred to as 60 wt% S-PAF-1-CHO@CS, 70 wt% S-PAF-1-CHO@CS, and 80 wt% S-PAF-1-CHO@CS, respectively.

3.2 Characterization of S-PAF-1-CHO@CS aerogel

The morphologies of S-PAF-1-CHO and the composite aerogels containing 60 wt%, 70 wt%, and 80 wt% S-PAF-1-CHO were examined by SEM. As shown in Figure S5, S-PAF-1-CHO consists of spherical particles with an average diameter of approximately 300 nm. In the SEM images of the composite aerogels (Figure 2a), the S-PAF-1-CHO particles are clearly embedded within the chitosan matrix. Moreover, as the S-PAF-1-CHO content increases, a greater fraction of

the chitosan surface is covered by the particles. The 80 wt% S-PAF-1-CHO@CS aerogel is extremely lightweight, with a density of 46 mg cm^{-3}, allowing it to stand stably on the filaments of a dandelion seed (Figure 2b). The mechanical properties of the S-PAF-1-CHO@CS aerogels were assessed by compressive stress–strain measurements. As shown in Figure 2c and Video 1, the 80 wt% S-PAF-1-CHO@CS aerogel fully recovers its shape after compression to 40% strain, which can be attributed to effective crosslinking within the composite network. The compressive stress–strain curves of the aerogels are presented in Figure 2d. At 40% strain, the compressive stresses of the 60 wt%, 70 wt%, and 80 wt% S-PAF-1-CHO@CS aerogels are 4.5, 8.7, and 29.4 kPa, respectively. The increase in stress with higher S-PAF-1-CHO loading indicates that the incorporation of S-PAF-1-CHO reinforces the mechanical strength of the composite aerogels. The BET surface area and porosity of S-PAF-1-CHO and the S-PAF-1-CHO@CS aerogels were characterized by nitrogen adsorption measurements (Figures 2e and S6). At low relative pressures, all four materials exhibit a sharp increase in nitrogen uptake due to micropore filling. The Brunauer-Emmett-Teller (BET) surface areas of S-PAF-1-CHO, 80 wt% S-PAF-1-CHO@CS, 70 wt% S-PAF-1-CHO@CS, and 60 wt% S-PAF-1-CHO@CS were calculated to be 3672, 2133, 1623, and 1092 $m^2 \cdot g^{-1}$, respectively. As shown in Table S1, the pore volumes calculated at P/P_0 = 0.99 are 2.3, 1.1, 0.8, and 0.6 $cm^3 \cdot g^{-1}$, respectively. The observed decrease in BET surface area and pore volume suggests that chitosan infiltrates the pore channels of S-PAF-1-CHO during aerogel fabrication, thereby reducing the internal porosity. From the pore size distribution curves (Figure S6), it can be seen that, compared with S-PAF-1-CHO, all three aerogels retain the original 1.4 nm pores while also exhibiting a new pore size at approximately 1.17 nm. This observation further confirms that chitosan partially infiltrates the internal pores of S-PAF-1-CHO. Compared with previously reported shaped materials for VOCs adsorption, 80 wt% S-PAF-1-CHO@CS not only achieves a high powder loading but also maintains a remarkably high BET surface area (Figure 2f). Thermogravimetric analysis (Figure S7) shows that the initial weight loss of the S-PAF-1-CHO@CS aerogels is attributed to the evaporation of residual water. The weight loss observed between 100-400 °C corresponds to the decomposition of surface functional groups, with the extent of mass reduction differing among the three composite aerogels due to their varying S-PAF-1-CHO contents. The weight loss above 400 °C is primarily attributed to the collapse of the polymer framework. The hydrophilicity and hydrophobicity of the samples were verified by water vapor adsorption tests, and the corresponding isotherms are displayed in Figure S8. PAF-1 shows extremely low water uptake over the full relative pressure range (P/P_0 = 0–1), confirming its intrinsic strong hydrophobicity. Although the chitosan matrix slightly elevates the hydrophilicity of the composites, the hydrophobic PAF-1 framework dominates the overall water adsorption behavior. The 80 wt% S-PAF-1-CHO@CS exhibits

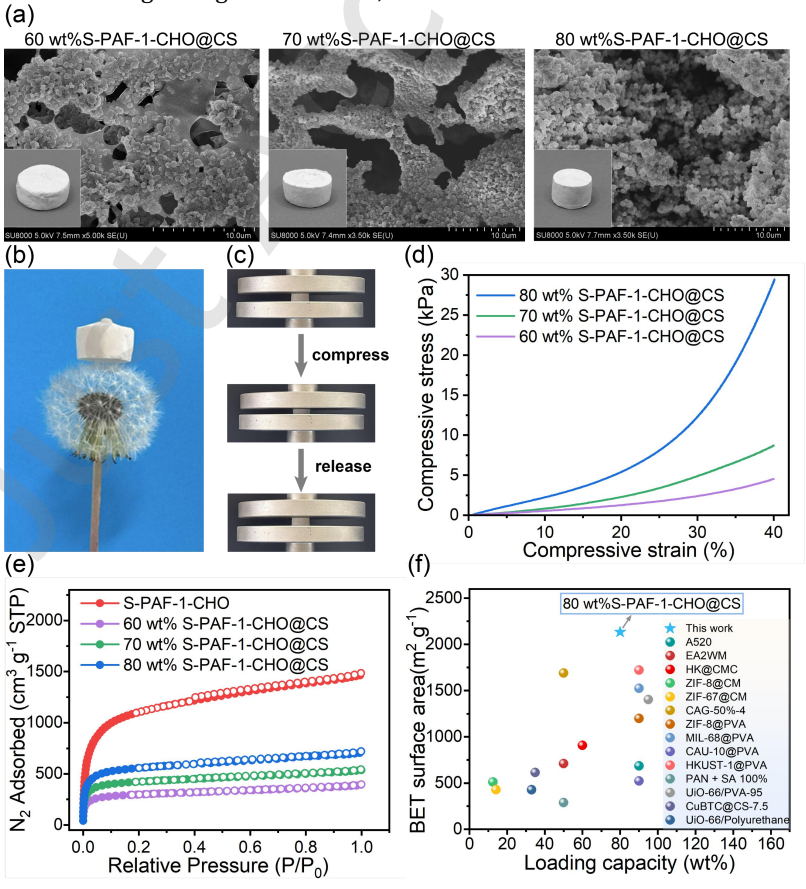

Figure 2. (a) SEM images and photographs of the 60 wt% S-PAF-1-CHO@CS, 70 wt% S-PAF-1-CHO@CS, and 80 wt% S-PAF-1-CHO@CS aerogels; (b) Photograph of the 80 wt% S-PAF-1-CHO@CS aerogel standing on a dandelion seed; (c) Photographs showing the recovery process of the 80 wt% S-PAF-1-CHO@CS aerogel after compression; (d) Stress-strain curves of the 60 wt%, 70 wt%, and 80 wt% S-PAF-1-CHO@CS aerogels under 40% compression; (e) N_2 adsorption – desorption isotherms of S-

PAF-1-CHO and a series of PAF-based aerogels at 77 K; (f) Comparison of powder loading capacity and BET surface area with other shaped materials in the VOCs adsorption field.3.3 VOCs adsorption and separation performance of S-PAF-1-CHO@CS

negligible water uptake in the typical atmospheric humidity range (P/P_0 = 0.3–0.7, 30–70% RH), which is far lower than the 60 wt% S-PAF-1-CHO@CS and 70 wt% S-PAF-1-CHO@CS. The high PAF loading effectively suppresses the accessibility of chitosan's hydrophilic groups, endowing the material with excellent moisture resistance and low water vapor sensitivity. This composite design integrates the structural advantages of chitosan and the superior hydrophobicity of PAFs, ensuring long-term stability in humid air and enabling reliable practical applications under real atmospheric conditions.

3.3 VOCs adsorption and separation performance of S-PAF-1-CHO@CS

To evaluate the VOCs adsorption performance of the PAF-based aerogels, the 80 wt% S-PAF-1-CHO@CS aerogel, which exhibits the highest BET surface area among the composites, was selected for adsorption tests using benzene, toluene, and cyclohexane as probes. The adsorption isotherms at 298 K are shown in Figure 3a. The adsorption capacities for all VOCs increase steadily with increasing pressure. At saturation, the aerogel exhibits the highest uptake for benzene, indicating its strong affinity toward this compound. Figure 3b compares the benzene adsorption isotherms of PAF-1 and 80 wt% S-PAF-1-CHO@CS at 298 K. Both materials exhibit a sharp increase in benzene uptake at low relative pressures ($P/P_0 < 0.05$), which can be attributed to the interactions between the aromatic rings of benzene and the aromatic framework of PAF-1. As the pressure increases, the benzene adsorption capacities of both materials continue to rise. At saturated vapor pressure, the benzene uptakes of PAF-1 and 80 wt% S-PAF-1-CHO@CS reach 23.69 mmol·g^{-1} and 20.49 mmol·g^{-1}, respectively. The higher benzene uptake of PAF-1 can be primarily attributed to its larger specific surface area. Compared with previously reported benzene adsorbents (Figure 3c), including MIL-101, MCM-41, and HKUST-1, PAF-1 exhibits the highest benzene adsorption capacity under saturated vapor pressure at 298 K [29-33]. Notably, although the 80 wt% S-PAF-1-CHO@CS composite is a monolithic material rather than a powder, it still exhibits excellent benzene uptake, exceeding that of many other powder-type porous adsorbents. To assess the dynamic adsorption performance of benzene at low concentrations, breakthrough experiments were carried out for PAF-1 and a series of PAF-based aerogels. In general, a longer breakthrough time indicates better dynamic adsorption capability. Figure 3d presents the benzene breakthrough curves of PAF-1 and the PAF-based aerogels at 298 K and 1 bar (with a benzene concentration of 2000 ppm balanced by He at a total flow rate of 25 mL min^{-1}). The monolithic 60 wt% S-PAF-1-CHO@CS, 70 wt% S-PAF-1-CHO@CS, 80 wt% S-PAF-1-CHO@CS, as well as powdered PAF-1, exhibit breakthrough times of 15, 23, 30, and 25 h g^{-1}, respectively. Notably, the breakthrough time of 80 wt% S-PAF-1-CHO@CS shows a longer breakthrough time than PAF-1, which can be attributed to the tendency of powdered PAF-1 to aggregate under dynamic gas flow, causing pore blockage and rapid saturation. In contrast, the chitosan matrix in 80 wt% S-PAF-1-CHO@CS effectively disperses and immobilizes the PAF-1 particles, preventing aggregation and maintaining accessibility of active adsorption sites during dynamic operation. Furthermore, the microporous structure of the composite provides rapid diffusion pathways for benzene molecules, reducing mass-transfer resistance and enabling faster transport to the microporous adsorption sites, thereby prolonging the breakthrough time. From these curves, benzene uptake was estimated to be 3.33 mmol g^{-1} for PAF-1 and 5.98 mmol g^{-1} for 80 wt% S-PAF-1-CHO@CS under a benzene concentration of 2000 ppm. This result is consistent with the trend observed in static adsorption measurements and further confirms that the newly introduced 1.17 nm micropores in the 80 wt% S-PAF-1-CHO@CS aerogel significantly enhance benzene adsorption at low concentrations.

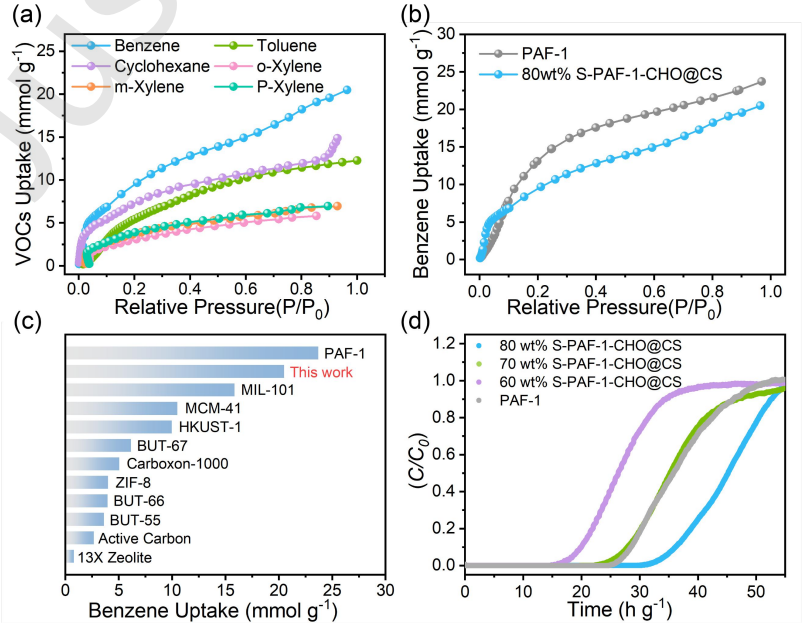

Figure 3. (a) VOCs adsorption isotherms of the 80 wt% S-PAF-1-CHO@CS aerogel at 298 K; (b) Benzene adsorption isotherms

of powder PAF-1 and monolithic 80 wt% S-PAF-1-CHO@CS at 298 K. (c) Comparison of benzene adsorption capacities with other reported adsorbents; (d) Benzene breakthrough curves of PAF-1 and the 60 wt%, 70 wt%, and 80 wt% S-PAF-1-CHO@CS aerogels at 298 K under dry conditions (2000 ppm benzene, balance He, with 25 mL min^{-1} flow-rate at 298 K and 1 bar

4 Conclusions

In this work, we developed a surface-modification strategy to functionalize PAF-1 with aldehyde groups, yielding S-PAF-1-CHO without losing the major porosity. This surface-functionalized powder was then integrated with chitosan to fabricate robust aerogels with S-PAF-1-CHO loadings as high as 80 wt%. The resulting monoliths not only overcome the practical handling issues of powders but also retain the exceptional benzene adsorption capacity of the parent PAF-1. Remarkably, dynamic breakthrough experiments with benzene vapor revealed that the 80 wt% aerogel surpasses the powder form in adsorption performance, underscoring its significant potential for practical benzene removal from air.

Electronic Supplementary Material: Supplementary material (Pore size distribution, TGA, SEM image, Stress-strain curves, Figs. S1–S8, Tables S1 and Video 1) is available in the online version of this article at https://doi.org/10.26599/NR.2026.94908747.

Data availability

All data needed to support the conclusions in the paper are presented in the manuscript and the Electronic Supplementary Material.

Acknowledgements

This work was supported by the National Natural Science Foundation of China (Grant No.: 92575203; 22575037), the "111" project (Grant No.: B18012), and the Project of Education Department of Jilin Province, China (Grant No.: JJKH20261645KJ). The authors also thank Jingwei Gaobo for assisting with the vapor breakthrough experiments.

Declaration of competing interest

All the contributing authors report no conflict of interests in this work.

Author contribution statement

Q. H. Y. W.: Data curation, project administration, validation, writing manuscript, experimental design. Y. Z.: Data curation. W. H.: Project administration. J. T. J.: Project administration, project design, funding acquisition, revising manuscript. G. S. Z.: Project administration, project design, funding acquisition, revising manuscript.

Informed consent

Not applicable.

Ethics statement

Not applicable.

Use of AI statement

None.

References

[1] Barea, E.;Montoro, C.; Navarro, J. A. R. Toxic gas removal – metal–organic frameworks for the capture and degradation of toxic gases and vapours. *Chem. Soc. Rev.* **2014**, *43*, 5419-5430.

[2] Faber, J.;Brodzik, K.;Gołda-Kopek, A.; Łomankiewicz, D. Benzene, toluene and xylenes levels in new and used vehicles of the same model. *Journal of Environmental Sciences* **2013**, *25*, 2324-2330.

[3] Wallington, T. J.;Anderson, J. E.;Dolan, R. H.; Winkler, S. L. Vehicle Emissions and Urban Air Quality: 60 Years of Progress. *Atmosphere* **2022**, *13*, 650.

[4] Kim, S.-J.;Kwon, H.-O.;Lee, M.-I.;Seo, Y.; Choi, S.-D. Spatial and temporal variations of volatile organic compounds using passive air samplers in the multi-industrial city of Ulsan, Korea. *Environ. Sci. Pollut. Res.* **2019**, *26*, 5831-5841.

[5] Saha, D.;Mirando, N.; Levchenko, A. Liquid and vapor phase adsorption of BTX in lignin derived activated carbon: Equilibrium and kinetics study. *J. Clean. Prod.* **2018**, *182*, 372-378.

[6] McHale, C. M.; Zhang, L.; Smith, M. T. Current understanding of the mechanism of benzene-induced leukemia in humans: implications for risk assessment. *Carcinogenesis* **2011**, *33*, 240-252.

[7] Yang, K.;Sun, Q.;Xue, F.; Lin, D. Adsorption of volatile organic compounds by metal–organic frameworks MIL-101: Influence of molecular size and shape. *J. Hazard. Mater.* **2011**, *195*, 124-131.

[8] Sui, H.;Liu, J.;He, L.;Li, X.; Jani, A. Adsorption and desorption of binary mixture of acetone and ethyl acetate on silica gel. *Chem. Eng. Sci.* **2019**, *197*, 185-194.

[9] Hussein, M. S.; Ahmed, M. J. Fixed bed and batch adsorption of benzene and toluene from aromatic hydrocarbons on 5A molecular sieve zeolite. *Mater. Chem. Phys.* **2016**, *181*, 512-517.

[10] Chingombe, P.;Saha, B.; Wakeman, R. J. Surface modification and characterisation of a coal-based activated carbon. *Carbon* **2005**, *43*, 3132-3143.

[11] Kim, K.-J.; Ahn, H.-G. The effect of pore structure of zeolite on the adsorption of VOCs and their desorption properties by microwave heating. *Micropor. Mesopor. Mater.* **2012**, *152*, 78-83.

[12] Das, D.;Gaur, V.; Verma, N. Removal of volatile organic compound by activated carbon fiber. *Carbon* **2004**, *42*, 2949-2962.

[13] Ben, T.;Ren, H.;Ma, S.;Cao, D.;Lan, J.;Jing, X.;Wang, W.;Xu, J.;Deng, F.;Simmons, J. M.;Qiu, S.; Zhu, G. Targeted Synthesis of a Porous Aromatic Framework with High Stability and Exceptionally High Surface Area. *Angew. Chem. Int. Ed.* **2009**, *48*, 9457-9460.

[14] Wang, Z.;Cao, C.;Jiang, L.;Xing, Z.;Jia, J.; Zhu, G. Near-Infrared Light Catalysis of Carbon Dioxide Reduction by Conjugated Porous Aromatic Frameworks. *Angew. Chem. Int. Ed.* **2025**, *64*, e202508924.

[15] Wang, Q.;Lin, L.;Jiang, L.;Wang, Z.;Zhang, Y.;Han, Q.;Huang, X.;Zhu, C.;Jia, J.;Bian, Z.; Zhu, G. A new post-synthetic route to graft amino groups in porous organic polymers for CO_2 capture. *Chem. Sci.* **2025**, *16*, 15121-15128.

[16] Zhang, Y.; Lin, L.; Wang, Z.; Zhao, Y.; Jiang, L.; Han, Q.; Gao, N.; Jia, J.; Feng, X.; Zhu, G. Fast responsive drug delivery device for thermo-triggered nitric oxide release by surface modified porous frameworks. *Nano Res.* **2025**, *18*, 94907227.

[17] Le, V. N.;Tu, T. N.; Kim, J. Facile synthesis of Cu-based metal–organic framework/chitosan composite granules for toluene adsorption. *Sep. Purif. Technol.* **2023**, *306*, 122718.

[18] Cui, X.;Sun, X.;Liu, L.;Huang, Q.;Yang, H.;Chen, C.;Nie, S.;Zhao, Z.; Zhao, Z. In-situ fabrication of cellulose foam HKUST-1 and surface

modification with polysaccharides for enhanced selective adsorption of toluene and acidic dipeptides. *Chem. Eng. J.* **2019**, *369*, 898-907.

[19] Pinto, M. L.;Dias, S.; Pires, J. Composite MOF Foams: The Example of UiO-66/Polyurethane. *ACS Appl. Mater. Interfaces* **2013**, *5*, 2360-2363.

[20] Jhinjer, H. S.;Singh, A.;Bhattacharya, S.;Jassal, M.; Agrawal, A. K. Metal-organic frameworks functionalized smart textiles for adsorptive removal of hazardous aromatic pollutants from ambient air. *J. Hazard. Mater.* **2021**, *411*, 125056.

[21] Le, V. N.;Kim, D.;Kim, J.; Othman, M. R. Freeze Granulation of Nanoporous UiO-66 Nanoparticles for Capture of Volatile Organic Compounds. *ACS Appl. Nano Mater.* **2021**, *4*, 8863-8871.

[22] So, P. B.;Liu, C.-Y.;Lai, Y.-L.;Lee, C.-S.; Lin, C.-H. MOF@PVA beads for dynamic and low concentration VOC capture. *Materials Advances* **2022**, *3*, 6458-6465.

[23] Yates, M.;Blanco, J.;Avila, P.; Martin, M. P. Honeycomb monoliths of activated carbons for effluent gas purification. *Micropor. Mesopor. Mater.* **2000**, *37*, 201-208.

[24] Yu, Y.;Ma, Q.;Zhang, J.-b.; Liu, G.-b. Electrospun SiO_2 aerogel/polyacrylonitrile composited nanofibers with enhanced adsorption performance of volatile organic compounds. *Appl. Surf. Sci.* **2020**, *512*, 145697.

[25] Zhang, L.;Sun, Q.;Su, T.;Wang, C.; Yang, Y. MOF-derived 3D porous carbon aerogels as an efficient adsorbent for toluene in humid air. *J. Environ. Chem. Eng.* **2021**, *9*, 106722.

[26] Guillerm, V.;Weseliński, Ł. J.;Alkordi, M.;Mohideen, M. I. H.;Belmabkhout, Y.;Cairns, A. J.; Eddaoudi, M. Porous organic polymers with anchored aldehydes: a new platform for post-synthetic amine functionalization en route for enhanced CO_2 adsorption properties. *Chem. Commun.* **2014**, *50*, 1937-1940.

[27] Yuan, Y.;Cao, D.;Cui, F.;Yang, Y.;Zhang, C.;Song, Y.;Zheng, Y.;Cao, J.;Chen, S.;Song, Y.;Wang, F.; Zhu, G. High-capacity uranium extraction from seawater through constructing synergistic multiple dynamic bonds. *Nat. Water* **2025**, *3*, 89-98.

[28] Zhao, R.;Ma, T.;Zhao, S.;Rong, H.;Tian, Y.; Zhu, G. Uniform and stable immobilization of metal-organic frameworks into chitosan matrix for enhanced tetracycline removal from water. *Chem. Eng. J.* **2020**, *382*, 122893.

[29] Jhung, S. H.;Lee, J.-H.;Yoon, J. W.;Serre, C.;Férey, G.; Chang, J.-S. Microwave Synthesis of Chromium Terephthalate MIL-101 and Its Benzene Sorption Ability. *Adv. Mater.* **2007**, *19*, 121-124.

[39] Xie, L.-H.;Liu, X.-M.;He, T.; Li, J.-R. Metal-Organic Frameworks for the Capture of Trace Aromatic Volatile Organic Compounds. *Chem* **2018**, *4*, 1911-1927.

[31] He, T.;Kong, X.-J.;Bian, Z.-X.;Zhang, Y.-Z.;Si, G.-R.;Xie, L.-H.;Wu, X.-Q.;Huang, H.;Chang, Z.;Bu, X.-H.;Zaworotko, M. J.;Nie, Z.-R.; Li, J.-R. Trace removal of benzene vapour using double-walled metal–dipyrazolate frameworks. *Nat. Mater.* **2022**, *21*, 689-695.

[32] Zhao, Z.;Wang, S.;Yang, Y.;Li, X.;Li, J.; Li, Z. Competitive adsorption and selectivity of benzene and water vapor on the microporous metal organic frameworks (HKUST-1). *Chem. Eng. J.* **2015**, *259*, 79-89.

[33] Wang, C.-M.;Chang, K.-S.;Chung, T.-W.; Wu, H. Adsorption Equilibria of Aromatic Compounds on Activated Carbon, Silica Gel, and 13X Zeolite. *J. Chem. Eng. Data* **2004**, *49*, 527-531.

Electronic Supplementary Material

Surface-engineered porous aromatic framework enables a monolithic aerogel for high-efficiency benzene adsorption

Qihaoyue Wang, Yao Zheng, Wei Hu, Jiangtao Jia, and Guangshan Zhu

Key Laboratory of Polyoxometalate and Reticular Material Chemistry of Ministry of Education, Faculty of Chemistry, Northeast Normal University, Changchun 130024, China

Address correspondence to Jiangtao Jia, jiangtaojia@nenu.edu.cn; Guangshan Zhu, zhugs@nenu.edu.cn

Supporting information to https://doi.org/10.26599/NR.2026.94908747

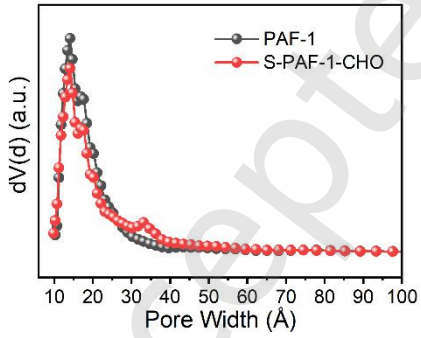

Figure S1. Pore size distribution of PAF-1, S-PAF-1-CHO based on nonlocal density functional theory (NLDFT) calculation.

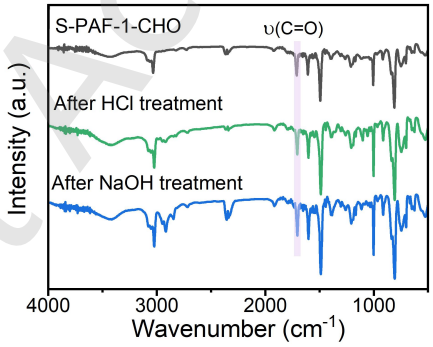

Figure S2. FT-IR spectra of S-PAF-1-CHO after acid and alkali treatments.

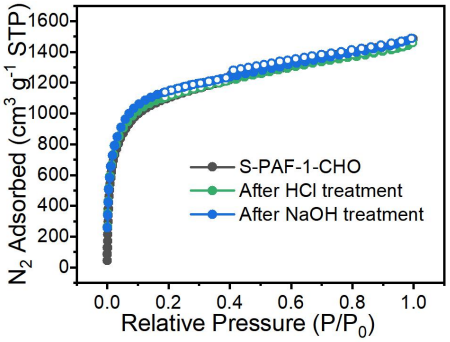

Figure S3. N_2 adsorption – desorption isotherms of S-PAF-1-CHO after acid and alkali treatments at 77K.

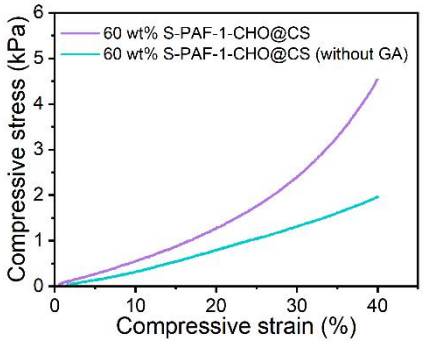

Figure S4. stress-strain curves of the 60 wt%S-PAF-1-CHO@CS aerogels and 60 wt%S-PAF-1-CHO@CS (without GA) under 40% compression.

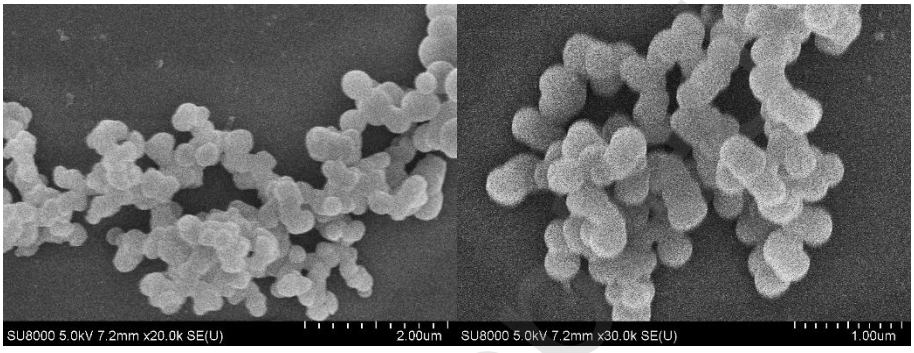

Figure S5. SEM images of the S-PAF-1-CHO.

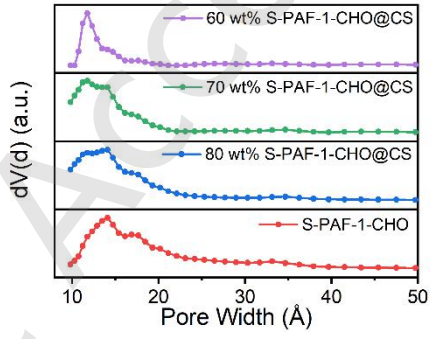

Figure S6. Pore size distribution of S-PAF-1-CHO, 60 wt% S-PAF-1-CHO@CS, 70 wt% S-PAF-1-CHO@CS and 80 wt% S-PAF-1-CHO@CS based on nonlocal density functional theory (NLDFT) calculation.

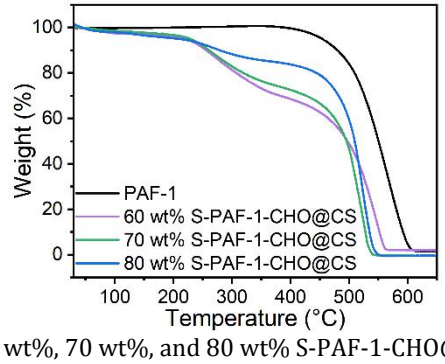

Figure S7. TGA curves of PAF-1 and the 60 wt%, 70 wt%, and 80 wt% S-PAF-1-CHO@CS aerogels.

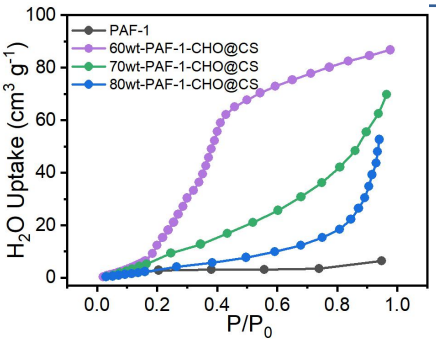

Figure S8. water vapor adsorption isotherms of PAF-1 and the 60 wt%, 70 wt%, and 80 wt% S-PAF-1-CHO@CS aerogels.

Table S1. Porosity of the S-PAF-1-CHO/CS aerogel series

	BET surface area [$m^2 g^{-1}$]	Pore width [nm]	Pore Volume [$cm^3 g^{-1}$]
S-PAF-1-CHO	3672	1.4	2.3
80wt%S-PAF-1-CHO@CS	2133	1.17/1.4	1.1
70wt%S-PAF-1-CHO@CS	1623	1.17/1.4	0.8
60wt%S-PAF-1-CHO@CS	1092	1.17/1.4	0.6

Video 1. Compression stress–strain testing process of the 80 wt% S-PAF-1-CHO@CS aerogel